



HAL
open science

Bayesian inversion of laboratory experiments of transport through limestone fractures

François Lehmann, Mohammad Mahdi Rajabi, Benjamin Belfort, Frederick Delay, Marwan Fahs, Philippe Ackerer, Anis Younes

► **To cite this version:**

François Lehmann, Mohammad Mahdi Rajabi, Benjamin Belfort, Frederick Delay, Marwan Fahs, et al.. Bayesian inversion of laboratory experiments of transport through limestone fractures. *Journal of Contaminant Hydrology*, 2022, 249, pp.104045. 10.1016/j.jconhyd.2022.104045 . hal-03851945

HAL Id: hal-03851945

<https://hal.science/hal-03851945v1>

Submitted on 14 Nov 2022

HAL is a multi-disciplinary open access archive for the deposit and dissemination of scientific research documents, whether they are published or not. The documents may come from teaching and research institutions in France or abroad, or from public or private research centers.

L'archive ouverte pluridisciplinaire **HAL**, est destinée au dépôt et à la diffusion de documents scientifiques de niveau recherche, publiés ou non, émanant des établissements d'enseignement et de recherche français ou étrangers, des laboratoires publics ou privés.

Research Article

Bayesian inversion of laboratory experiments of transport through limestone fractures

François Lehmann¹, Mohammad Mahdi Rajabi^{2,*}, Benjamin Belfort¹, Frederick Delay¹,
Marwan Fahs¹, Philippe Ackerer¹, Anis Younes¹

¹*Institut Terre et Environnement de Strasbourg, UMR7063 CNRS/Université de Strasbourg
/ENGEES 67084 Strasbourg, France.*

²*Faculty of Civil and Environmental Engineering, Tarbiat Modares University, Tehran, Iran*

Submitted to Journal of Contaminant Hydrology

* Contact Person: Mohammad Mahdi Rajabi

E-mail: mmrajabi@modares.ac.ir

1. Introduction

1
2 It is estimated that up to a quarter of the world's population depends on karstic aquifers of
3
4 mostly limestone nature, for water supply (Ford and Williams, 2013). Fracture (or conduit)
5
6 networks are generally considered the dominant flow and transport pathways in limestone
7
8 media, because limestone matrix permeability and porosity are low, and secondary permeability
9
10 is high (Florea and Wicks, 2001). Water and contaminants travel at much greater speeds within
11
12 the fracture networks compared with the surrounding porous limestone matrix (Li et al., 2008),
13
14 which renders limestone aquifers highly vulnerable to contamination (Morales et al., 2007). In
15
16 the past three decades, numerous studies have provided insights into flow dynamics and
17
18 transport mechanisms in limestone fractured systems. These studies have mostly concluded that
19
20 accurate simulation of water and contaminant movement in fractured limestone is complicated
21
22 by the uncertainty of characterizing fracture properties (Qian et al., 2005). This uncertainty
23
24 stems from the high spatial variability of fracture properties, and the lack of direct
25
26 measurements methods (Wang et al., 2017).
27
28
29
30
31
32

33
34 Breakthrough curves (BTCs), obtained from dye or salt tracer tests, are useful for the estimation
35
36 of model parameters (Jørgensen et al., 2004; Helmke et al., 2005) and/or the characterization
37
38 of fracture properties (Goldscheider and Drew, 2014; Zhao et al., 2017). The approach often
39
40 consists of employing an inverse method based on optimization or inference processes, to fit
41
42 observed and model-simulated BTCs. Various fracture parameters, such as effective porosity,
43
44 aperture, length, roughness, density, and network patterns can affect the shape of BTCs
45
46 (Mohammadi et al., 2019), and thus could be estimated from them. BTCs can also be employed
47
48 for estimating contaminant transport parameters in fractured media, such as dispersivity,
49
50 retardation and degradation, as well as the characterization of conduit-matrix interactions
51
52 (Goldscheider et al., 2008). Key inverse methods in this context include gradient-based
53
54 minimization (e.g. Abdelaziz and Merkel, 2015; Hawkins et al., 2020) and sample-based
55
56
57
58
59
60

1 Bayesian inference such as Markov chain Monte Carlo (MCMC) (e.g. [Somogyvári et al., 2017](#);
2 [Zhou et al., 2021](#)).

3
4 However, estimating fracture parameters from BTCs is not a straightforward task ([Hartmann et](#)
5 [al., 2014](#)). On the one hand, the operation is prone to common inverse modeling challenges
6
7 such as conceptual model uncertainty, instability, ill-posedness, non-convergence, non-unique
8
9 and non-optimal solutions ([Wang et al., 2017](#); [Rajabi et al., 2018](#)). On the other hand, BTCs
10
11 may exhibit asymmetry with long tails ([Massei et al., 2006](#); [Labat and Mangin, 2015](#); [Fiori and](#)
12 [Becker, 2015](#)) or multiple peaks due to factors such as the strong heterogeneity of limestone
13
14 aquifers, the presence of pools along main fractures and multiple flow paths ([Hauns et al., 2001](#);
15
16 [Wang et al., 2020](#)). Capturing such complicated BTCs has proven problematic, which affects
17
18 the choice of the modeling approach ([Field and Leji, 2012](#)). Partitioning models are often used
19
20 to simulate such BTCs, but these models require a large number of parameters ([Zoghbi and](#)
21 [Basha, 2020](#)). Bearing in mind that not all parameters are of equal importance with respect to
22
23 sensitivities of BTCs, determining the most significant factors so as to limit the number of
24
25 parameters is necessary ([Li et al., 2019](#)).

26
27 Different approaches have been explored for fracture parameter estimation from BTCs. Most
28
29 previous studies in this context are based on ‘hypothetical’ examples (e.g. [Somogyvári et al.,](#)
30 [2017](#); [Zhou et al., 2021](#)). This is a key shortcoming, as hypothetical examples often lack the
31
32 complexity of real-world problems, and are limited to what the chosen numerical modeling
33
34 approach can reproduce. Moreover, the true values of fracture parameters are often not known
35
36 at the field-scale, thus rendering method validation using field-scale data often impractical. As
37
38 a consequence, bench-scale laboratory experiments under controlled conditions are important
39
40 for testing the validity of these inversion methods ([Pastore, 2018](#)). The fact that there are few
41
42 laboratory-based studies in this context can be mainly attributed to the difficulty of the
43
44 experimental process, as laboratory models must reflect a reduction in the scale of the physical
45
46
47
48
49
50
51
52
53
54
55
56
57
58
59
60

1 parameters and dimensions while maintaining similar forces (Zhang et al., 2016), the latter often
2 being represented by Reynolds, Froude and Peclet dimensionless numbers for flow and solute
3 transport in fractured media (Palmer 1999; Florea and Wicks, 2001).
4

5
6 Among the reported laboratory-scale studies, most have focused on the understanding of BTCs
7 and the relevant flow and transport processes. Examples include the study of scale effects on
8 BTCs by Hauns et al. (2001), interaction and mass transfer between a single conduit and its
9 bounding porous medium by Li (2004), sequestration mechanisms including the exchange of
10 water and solute between conduits and porous matrix by Li et al. (2008), empirical models of
11 water hydraulic head under different hydrological conditions by Zhang et al. (2016), and the effect
12 of variations in hydraulic gradient and conduit systems on BTCs by Mohammadi et al. (2019). In
13 these and other similar studies, analyzing flow and solute transport within a single or a two-
14 fracture system often forms the basis for studying complex fracture networks (Liu et al 2021).
15 The estimation of limestone fracture parameters using laboratory-scale models for method
16 analysis and validation often relies upon single or dual pipes made of silicon or PVC to model
17 the fractured medium (Field and Leji, 2012; Zhao et al., 2019; Wang et al., 2020). These studies
18 use nonlinear least-squares estimation or the MCMC method for the estimation of fracture
19 parameters.
20

21
22 Realistic laboratory experiments have been conducted by Jørgensen et al. (2004) for bromide
23 transport through undisturbed soil columns containing a high number of macropores (fractures
24 and biopores). In this study, the measured BCTs were used to assess the suitability of different
25 modeling approaches for the simulation of flow and transport in clayey till. Likewise, Helmke
26 et al. (2005) compared different modeling approaches to simulate solute transport through
27 fractures in a laboratory column of till. Their results showed that the different modeling
28 approaches employed could satisfactorily reproduce the observed BTCs, which suggests that
29 more elaborate models do not necessarily render more accurate results.
30
31
32
33
34
35
36
37
38
39
40
41
42
43
44
45
46
47
48
49
50
51
52
53
54
55
56
57
58
59
60
61
62
63
64
65

1 The simplest way for modeling flow and transport in fractured-porous media is based on the
2 equivalent porous medium (EPM) approach in which the fractured porous medium is replaced
3
4 by an equivalent porous medium with the same hydraulic conductivity (Helmke et al., 2005).
5
6 However, the most common models for the simulation of flow and transport in fractured porous
7
8 media are the discrete fracture and double porosity models (Jørgensen et al., 2004 ; Helmke et
9
10 al., 2005; Nikan et al., 2020). Some sophisticated variants also exist such as the triple continuum
11
12 models (Wu et al., 2004), the multi-rate mass transfer models (Guo et al., 2020) or the fractal
13
14 mobile/immobile models (Nikan et al., 2020).
15
16
17
18

19 The mobile/immobile (MIM) model is based on the dual porosity approach and considers the
20
21 fractures as the mobile region and the matrix as the immobile region. Advection and dispersion
22
23 occur exclusively in the mobile region, and the immobile region is a sink that stores the solute.
24
25 The exchange between the mobile and the immobile regions is often ruled by a first-order (FO)
26
27 mass transfer coefficient approach (Coats and Smith 1964). The resulting model has been
28
29 widely used for flow and transport in fractured porous media because of its simplicity compared
30
31 to discrete fracture models. Indeed, the latter require that the location, shape, orientation, size,
32
33 aperture, and hydraulic and solute transport properties of each fracture to be explicitly specified
34
35 as model inputs.
36
37
38
39
40

41 The objective of the present work is threefold. First, we aim at developing a novel experimental
42
43 setup for the study of transport through limestone fractures using salt tracer BTCs. The
44
45 proposed bench-scale setup includes multiple fractures, and is based on real limestone beams.
46
47 These features are novel compared to previous work. Second, we validate and analyze the
48
49 results of an inverse method using laboratory-scale data obtained under controlled conditions.
50
51 Third, we investigate the degree to which three transport models can reproduce the experimental
52
53 results under different (slow, medium, and fast) flow conditions. The first transport model,
54
55 named ADE, is based on the EPM approach and corresponds to the linear advection dispersion
56
57
58
59
60

1 equation. The second model, named FOMIM (first-order mobile-immobile), is based on the
2 MIM approach relying upon a linear first-order transfer function between mobile and immobile
3 zones. For its part, the third model, named NLMIM (non-linear mobile-immobile), uses a
4 nonlinear transfer function between the fractures and the matrix.
5
6
7

8
9 The structure of the paper is as follows. In Section 2 we describe the experimental setup, and
10 then briefly explain the three transport models. Section 2 also includes a description of the
11 inverse method employed. Then, the experimental BTCs and the simulation results of the BTCs
12 are presented and analyzed in Section 3. The paper is complemented in Section 4 by a review
13 of our main findings and prospects for future research.
14
15
16
17
18
19
20
21

22 **2. Materials and Methods**

23 **2.1. Laboratory Experiment**

24
25 A fractured porous medium is constructed at the laboratory scale using a column of inner
26 diameter $d_c = 6\text{ cm}$ and length $L_c = 15\text{ cm}$ filled with glass beads and small parallelepiped-
27 shaped limestone beams. The limestone used for the experiment is mainly composed of
28 dolomite ($\text{CaMg}(\text{CO}_3)_2$). The porous medium is composed of silicon dioxide beads (SiLibeads
29 Glass beads Type S N°4503, Sigmund Lindner) of 0.75 to 1.00 mm in diameter with a bulk
30 density of 1510 kg/m^3 . Small parallelepiped-shaped limestone beams of 1 cm^2 section and 4
31 to 5 cm length are placed inside the porous medium as shown in **Fig. 1a**.
32
33
34
35
36
37
38
39
40
41
42
43
44

45 The column shell (**Fig. 1b**) is a Plexiglas tube with the top and bottom end-plate assemblies
46 held together with 3 threaded rods. Each end-plate assembly has one access port in its center,
47 with a diameter $d_p = 6\text{ mm}$ and a perforated plate to support the porous medium and distribute
48 the flow over the entire column section. At the top and bottom end plates, two electrical
49 conductivity (EC) meters were used to continuously record (at 10 s time steps) the inlet and
50 outlet concentrations. The two EC meters were calibrated against standard solutions, which
51
52
53
54
55
56
57
58
59
60
61
62
63
64
65

allows for accurate (and reproducible) measurements of the EC. The injected aqueous solution is made of deionized water supplemented with sodium chloride (NaCl) at 2g/l. This mixture allows for obtaining a solution with a significant sensitivity of EC to the concentration, while density variations remain negligible. The column is mounted vertically with flow from bottom to top assured by a peristaltic pump. The flow rate was regularly controlled by weighing the cumulative outflow.

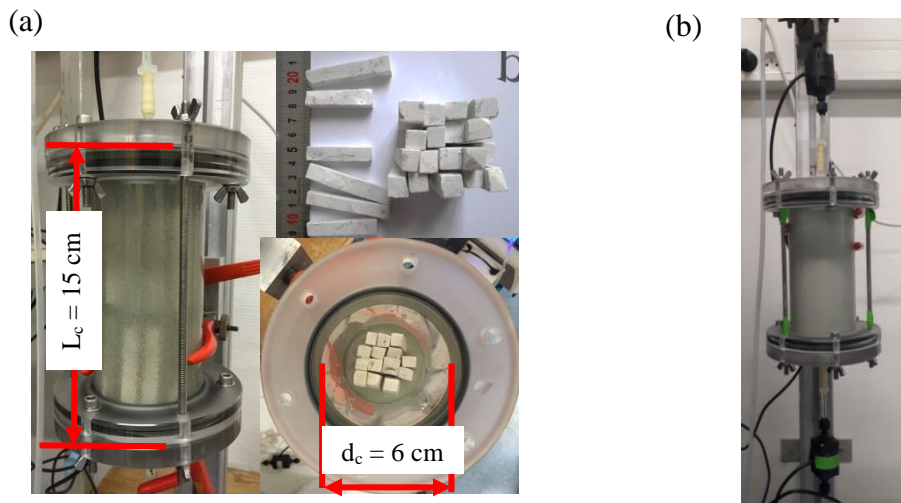


Figure 1. The laboratory experiment setup: (a) Plexiglas flow cell (inner diameter $d_c = 6$ cm and length $L_c = 15$ cm) used for the column experiment with glass beads of 1 mm diameter and limestone beams of 1 cm² section and 4 to 5 cm length, and (b) the column shell with the top and bottom end-plate assemblies.

Three experiments were performed under fast, medium, and slow flow velocities through the column corresponding to injected flow rates of $Q_{in} = 20.0, 2.0,$ and 0.2 ml/min, respectively.

Each experiment was repeated three times.

2.2. Mathematical Models

Three models are investigated to simulate transport through the column. The first model assumes an EPM, thus the transport through the column can be ruled by the following linear

ADE:

$$\frac{\partial C}{\partial t} = \frac{\partial}{\partial z} \left(D \frac{\partial C}{\partial z} \right) - \frac{\partial}{\partial z} (UC) \quad (1)$$

where $C [-]$ is the non-dimensional (normalized) concentration, $D = \alpha_L U + d_m [L^2T^{-1}]$ is the dispersion coefficient, $U [LT^{-1}]$ is the fluid velocity, d_m is the molecular diffusion coefficient assigned a small value of $5 \times 10^{-10} \text{ m}^2/\text{s}$ (as a common value in the literature), and $\alpha_L [L]$ is the dispersivity coefficient.

The second transport model FOMIM is based on the MIM approach and assumes a first-order mass transfer between the fractures and the matrix:

$$\begin{cases} \frac{\partial C_m}{\partial t} + \frac{\partial C_{im}}{\partial t} + \frac{\partial}{\partial z} (UC_m) - \frac{\partial}{\partial z} \left(D \frac{\partial C_m}{\partial z} \right) = 0 \\ \frac{\partial C_{im}}{\partial t} = \alpha (C_m - C_{im}) \end{cases} \quad (2)$$

where C_m and C_{im} stand for the (normalized) concentrations in the mobile and immobile phases, respectively, $\alpha [T^{-1}]$ is the first-order mass transfer coefficient between the fractures and the matrix (Coats and Smith 1964). It is worth noting that the coefficient α can be dependent on the mean flow velocity, as shown in Brissaud et al. (1978) and Herr et al. (1989).

The third transport model uses the MIM approach but assumes a nonlinear transfer function between the mobile and the immobile continuums as:

$$\frac{\partial C_{im}}{\partial t} = \frac{\lambda}{(1 + \mu C_m)^2} \quad (3)$$

where $\lambda [T^{-1}]$ and $\mu [-]$ are parameters of the nonlinear transfer function.

For the three transport models, initial conditions correspond to a zero solute concentration inside the column. The lower boundary ($z=0$) corresponds to a Dirichlet condition with the

1 normalized concentration fixed to one during solute injection, and to zero during clean water
2 injection. The upper boundary condition ($z=L$) corresponds to a null concentration gradient.
3
4

5 **2.3. Numerical Solutions**

6

7 The transport equation for both models is solved using the Discontinuous Galerkin (DG)
8 method. Usually, transport at small scales under pressure gradients (e.g., laboratory-scale
9 experiments) is advection-dominated, making the differential transport equations to become
10 hyperbolic (Godlewski and Raviart, 1996). Those are characterized by moving sharp fronts that
11 classical numerical methods (such as finite element or finite volume methods) fail to capture,
12 with the result of solutions plagued by non-physical oscillations and/or numerical diffusion
13 (Huyakorn and Pinder, 1983). For its part, the DG method leads to a robust and accurate
14 numerical scheme for problems involving sharp fronts (Tu and Aliabadi, 2005). The DG
15 method yields a highly-resolved scheme, which maintains the local mass conservation of finite
16 volume (FV) methods but also allows for high-order approximations (Kirby, 2000). When
17 applied to hyperbolic systems, the DG method is clearly superior to finite element methods
18 (Siegel et al, 1997; Arnold et al., 2002).
19
20
21
22
23
24
25
26
27
28
29
30
31
32
33
34
35
36

37 The transport equation is solved with the explicit upwind DG scheme. The stability of the
38 scheme, is ensured by the use of a suitable slope limiter to damp out the spurious oscillations
39 produced close to discontinuities or strong gradients of the approximate solution (Younes et al.,
40 2010). The obtained scheme is “total variation diminishing” and stable for Courant-Friedrichs-
41 Lewy (CFL) numbers equal or less than 0.5.
42
43
44
45
46
47
48

49 We use a linear discontinuous approximation of the concentration at each element. The degrees-
50 of-freedom are the mean and the first spatial derivative of the concentration inside each element.
51
52 This choice allows for an easy and efficient combination between the DG method for advection
53 and the FV method for dispersion without resorting to any operator splitting (Younes and
54 Ackerer, 2008). For the nonlinear transport problem (model NLMIM), a Newton–Raphson
55
56
57
58
59
60
61
62
63
64
65

1 algorithm is employed with a precision of 10^{-7} . The time step length is managed using the
2 Richardson extrapolation, that is an adaptive time-stepping procedure based on the posteriori
3 error estimate (Fahs et al., 2008).
4
5

6 **2.4. Bayesian Parameter Inference and Model Selection**

7
8
9 The vector of observations y_{mes} consists of the outflow EC measured at different times, for the
10 three (fast, medium, and slow) experiments assembled within the same “synthetic” transport
11 scenario of successive mass transfer at diverse velocities. All the parameters of the ADE model
12 of Eq. (1), the FOMIM transport model of Eq. (2) and the NLMIM model of Eq. (3) are assumed
13 unknowns, and sought by inverse modeling. In the case of the ADE transport model, the vector
14 of unknown parameters is $\xi = (U_1, U_2, U_3, \alpha_L)$ where U_1, U_2 and U_3 are the fluid velocity for
15 the fast, medium and slow flow rate experiments, respectively, and α_L is the dispersivity,
16 assumed to be independent of the fluid velocities in all three experiments. Initially, the
17 parameters of the model are assumed uniformly distributed over the large intervals reported in
18 the second and third columns of **Table 1**.
19
20
21
22
23
24
25
26
27
28
29
30
31
32
33
34

35 Regarding the FOMIM transport model, the coefficient α is considered as varying with the
36 fluid velocity in the column (Herr et al., 1989), thus resulting in three sought coefficients (one
37 per transport experiment). The vector of unknowns becomes $\xi = (U_1, U_2, U_3, \alpha_1, \alpha_2, \alpha_3, \alpha_L)$.
38
39
40
41
42
43

44 For the last NLMIM transport model, two cases are investigated. In the first case, the vector of
45 unknown parameters is $\xi = (U_1, U_2, U_3, \lambda, \mu, \alpha_L)$ where λ and μ are the transfer coefficients,
46 assumed to be similar for all three experiments. In the second case, the coefficient λ is
47 considered as varying with the fluid velocity in the column, thus resulting in a vector of
48 unknowns as $\xi = (U_1, U_2, U_3, \lambda_1, \lambda_2, \lambda_3, \mu, \alpha_L)$.
49
50
51
52
53
54
55
56

57 The parameters are estimated via a Bayesian approach combining the prior parameter
58 information with the observations to determine the posterior probability distribution functions
59
60
61
62
63
64
65

(PDFs) of model parameters. We rely upon the Markov chain Monte Carlo technique (MCMC) which has also been widely used by several authors in Hydrogeology (e.g. [Rajabi and Ataie-Ashtiani, 2016](#); [Moreira et al., 2016](#); [Younes et al., 2016](#); [Linde et al., 2017](#); [Wang et al. 2020](#)). MCMC generates random sequences of parameter sets, which converge asymptotically toward the target distribution. The statistical measures (e.g., mean and standard deviation) from the obtained distributions can then be used to estimate the mean parameter values and their confidence intervals to characterize parameter uncertainty. Using the Bayes theorem, the posterior density function of the parameters conditioned onto observations is as follows ([Gelman et al., 1995](#)):

$$p(\xi | \mathbf{y}_{mes}) \propto p(\mathbf{y}_{mes} | \xi) p(\xi) \quad (4)$$

in which $p(\mathbf{y}_{mes} | \xi)$ is the likelihood function measuring how well the model outputs are in agreement with the observations \mathbf{y}_{mes} , and $p(\xi)$ is the prior PDF of ξ , which encapsulates any prior knowledge about the unknown parameters.

In this work, the prior distributions for all parameters are assumed independent from one another and uniform. Further, large prior intervals are chosen for all parameters due to lack of knowledge of model parameter values. Error measurements of the output concentrations are assumed to be normally and independently distributed with zero mean and standard deviation equal to $\sigma_c = 0.02$ (for normalized concentrations bounded between 0 and 1).

Setting the calibration problem in a Bayesian framework yields the following posterior PDF:

$$p(\xi / \mathbf{y}_{mes}) \propto \sigma_c^{-N_c} \exp\left(-\frac{SS_C(\xi)}{2\sigma_c^2}\right) \quad (5)$$

where $SS_C(\xi) = \sum_{k=1}^{N_c} (C_{mes}^{(k)} - C_{mod}^{(k)}(\xi))^2$ is the sum of the squares of differences between the observed and predicted concentrations, $C_{mes}^{(k)}$ is the observed and $C_{mod}^{(k)}$ is the predicted output

1 concentrations at time t_k , and N_C , is the overall number of observed concentrations for the
 2 three experiments.
 3

4 The MCMC sampler generates a new candidate ξ^i from a proposal distribution $q(\xi^i | \xi^{i-1})$,
 5 which only depends on the previous accepted candidate. The new candidate can be accepted or
 6 rejected depending on the Hasting ratio α_H :
 7
 8
 9
 10
 11
 12

$$13 \alpha_H = \min \left(1, \frac{p(\xi^i / \mathbf{y}_{mes}) q(\xi^{i-1} | \xi^i)}{p(\xi^{i-1} / \mathbf{y}_{mes}) q(\xi^i | \xi^{i-1})} \right) \quad (6)$$

14 In this work, we use the DREAM_(ZS) MCMC sampler (Vrugt et al., 2003) with three parallel
 15 chains. The results are considered stationary if the chains are not auto-correlated and if the
 16 Gelman and Ruban (1992) criterion is verified ($R_{stat} \leq 1.2$). The set of parameters
 17 corresponding to the Maximum a Posteriori (MAP) value is then defined as:
 18
 19
 20
 21
 22
 23
 24
 25
 26
 27
 28
 29

$$30 \xi^{MAP} = \arg \max_{\xi} (p(\xi / \mathbf{y}_{mes})) \quad (7)$$

31 The Bayesian information criterion (BIC), used for the selection of the best model is defined as
 32 (Schwarz, 1978):
 33
 34
 35
 36
 37
 38

$$39 BIC = -2 \ln (p(\xi^{MAP} | \mathbf{y}_{mes})) + K \ln (N_C) \quad (8)$$

40 where K is the total number of estimated parameters and $p(\xi^{MAP} / \mathbf{y}_{mes})$ is the parameter density
 41 function evaluated at the MAP estimate (Schöniger et al., 2014). Since each error has a non-
 42 correlated (with the others) normal distribution: $N(0, \sigma_C^2)$, it follows that (Zhu et al., 2009):
 43
 44
 45
 46
 47
 48
 49
 50
 51

$$52 p(\xi^{MAP} | \mathbf{y}_{mes}) = \prod_{i=1}^{N_C} \frac{1}{\sigma_C \sqrt{2\pi}} \exp \left[-\frac{(C_i^{mes} - C_i^{mod}(\xi^{MAP}))^2}{2\sigma_C^2} \right] \quad (9)$$

3. Results and Discussion

3.1. Experimental BTCs

The measured breakthrough curves at the outlet are depicted in **Fig. 2** for the various experiments. Each of the fast (**Fig. 2a**), medium (**Fig. 2b**), and slow (**Fig. 2c**) flow rate experiment has been repeated three times. The results of **Fig. 2** show a very good reproducibility of the experiments (repeating three times the same experiment results in almost similar breakthrough curves). It is worth noting that the breakthrough curves in **Fig. 2** show a significant tail for the slow flow rate experiment (**Fig. 2c**). The tail is moderate with the medium flow experiment (**Fig. 2b**) and almost inexistent with the fast flow rate experiment (**Fig. 2a**).

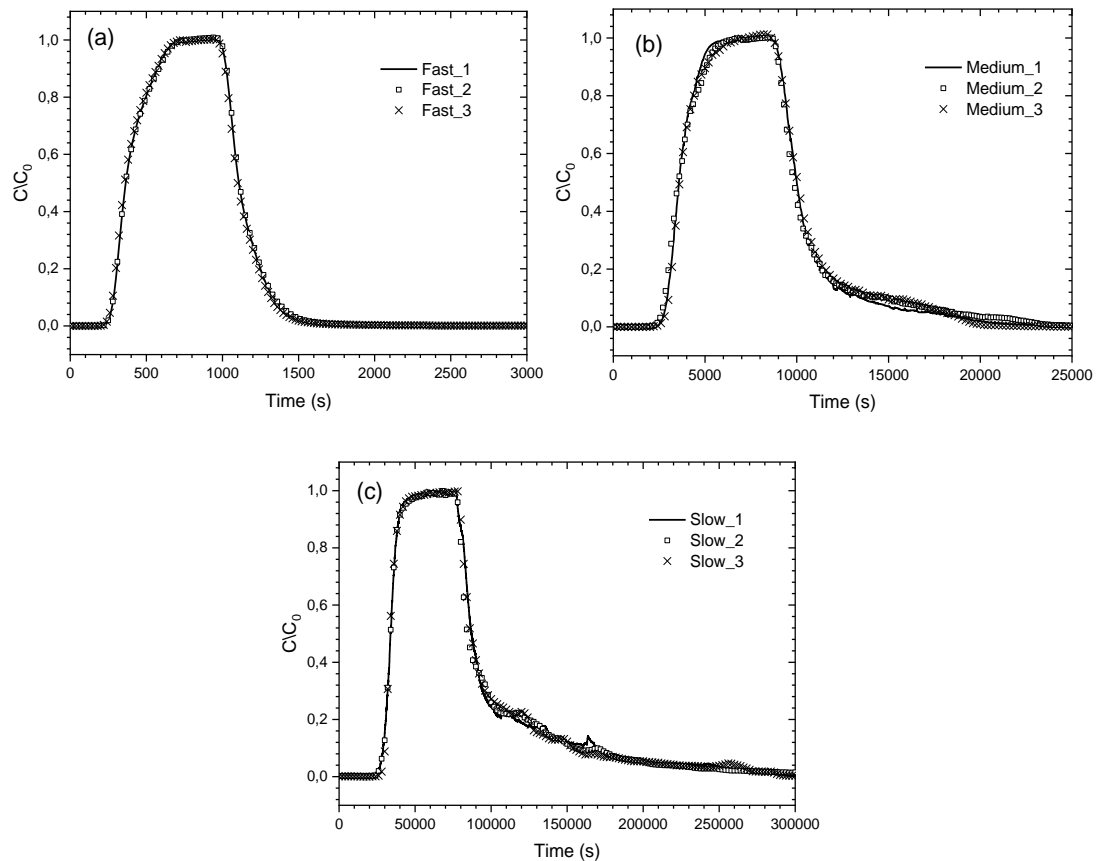


Fig. 2. Breakthrough curves for fast (a), medium (b), and slow (c) flow rates through the column, each of the experiments repeated three times.

3.2. Parameter Estimation for the ADE Model

For the ADE model, the MCMC sampler reaches convergence after 15,000 model runs. The results of Bayesian inversion are illustrated in **Fig. 3**. The diagonal plots show the posterior parameter distributions, whereas the off-diagonal plots display the pairwise correlations within the MCMC samples. Given the round-shaped patch delineated by pairwise correlations, there is almost no correlation between the four parameters, and all parameters show bell-shaped posterior distributions in the diagonal plots of **Fig. 3**.

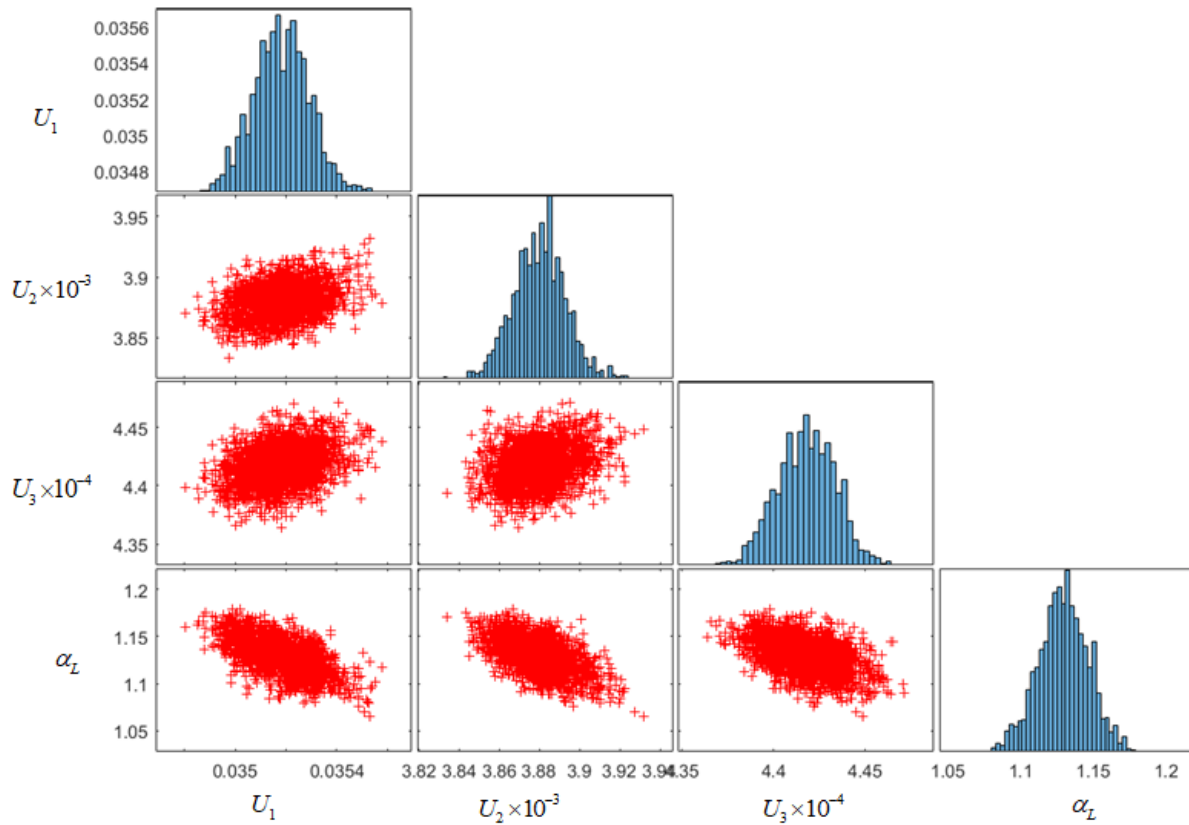


Fig. 3. MCMC solution for the ADE model. The diagonal plots represent the posterior distribution of the parameters. The off-diagonal scatterplots represent the correlations in the MCMC draws.

Table 1. Prior intervals, estimated mean values and confidence intervals (CIs) for the parameters of the ADE model.

Parameter	Prior intervals		Estimations		
	Lower bound	Upper bound	Mean	Standard deviation	95% Confidence Interval
U_1 [cm/s]	0.03	0.1	0.0352	$1.1 \cdot 10^{-4}$	(0.0350-0.0354)
U_2 [cm/s]	0.003	0.01	0.0039	$1.23 \cdot 10^{-5}$	(0.00385-0.00390)
U_3 [cm/s]	0.0003	0.001	$4.42 \cdot 10^{-4}$	$1.56 \cdot 10^{-6}$	(0.000439-0.000445)
α_L [cm]	0.0	3.0	1.13	0.017	(1.096-1.163)

The results of the Bayesian calibration (transport parameters in **Table 1**) show that the four parameters are well-estimated with narrow confidence intervals. **Fig. 4** depicts the measured output concentrations as well as the calibrated concentrations and the predictive uncertainty. In this figure, the green region represents the total predictive uncertainty which accounts for both the parametric uncertainty and measurement errors. **Fig. 4a** shows that the first experiment with the fast flow rate is well reproduced by the ADE model. Nevertheless, discrepancies between simulated and observed output concentrations can be observed for the second experiment (**Fig. 4b**). These discrepancies increase especially for the last experiment (**Fig. 4c**) dealing with the slow flow rate, with noticeable errors mainly in the leaching phase. The tails observed on the measured breakthrough curves for the medium- and slow-velocity experiments cannot be reproduced by the ADE transport model. The sum of the squared differences between the observed and predicted concentrations using parameters corresponding to the MAP and the BIC values are given in the **Table 2**.

Table 2. The total number of estimated parameters (K), the squared differences between the observed and predicted (using parameters of MAP) concentrations, and BIC for the ADE, FOMIM and NLMIM models.

Modeling Approach	K	$\sum_{i=1}^{N_C} (C_i^{mes} - C_i^{mod}(\xi^{MAP}))^2$	BIC
ADE	4	6.12	9173.96
FOMIM (variable α)	7	5.66	8044.77
NLMIM-Scenario 1	6	3.59	2862.83
NLMIM– Scenario 2 (variable λ)	8	0.6162	-4557.80

1
2
3
4
5
6
7
8
9
10
11
12
13
14
15
16
17
18
19
20
21
22
23
24
25
26
27
28
29
30
31
32
33
34
35
36
37
38
39
40
41
42
43
44
45
46
47
48
49
50
51
52
53
54
55
56
57
58
59
60
61
62
63
64
65

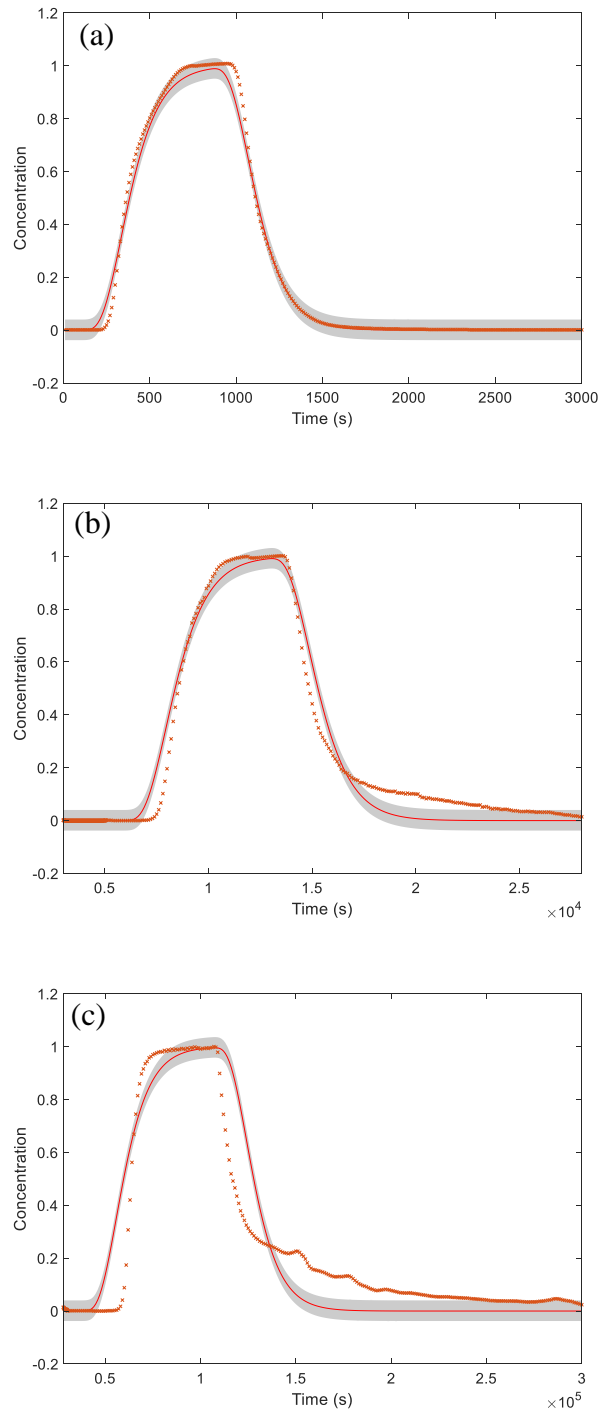


Fig. 4. Observed concentrations (dots), calibrated solution corresponding to the MAP (lines), and predictive uncertainty (grey band) with the ADE model for the fast (a), medium (b), and slow (c) flow rate experiments.

3.3 Parameter Estimation for the FOMIM Model

The FOMIM includes a mobile and an immobile phases with a linear transfer function between phases. Three transfer coefficients α are calibrated corresponding to the fast, medium and slow flow rate experiments. The three transfer coefficients have prior uniform distributions over large intervals (between 0 and 100, see **Table 3**).

Table 3. Prior intervals, estimated mean values and confidence intervals (CIs) for the parameters of the FOMIM model.

Parameters	Prior intervals		Estimations		
	Lower bound	Upper bound	Mean	Standard deviation	95% Confidence Interval
U_1 [cm/s]	0.03	0.1	$7.24 \cdot 10^{-2}$	$2.14 \cdot 10^{-4}$	$(7.19 \cdot 10^{-2} - 7.28 \cdot 10^{-2})$
U_2 [cm/s]	0.003	0.01	$8.0 \cdot 10^{-3}$	$2.51 \cdot 10^{-5}$	$(7.94 \cdot 10^{-3} - 8.05 \cdot 10^{-3})$
U_3 [cm/s]	0.0003	0.001	$8.73 \cdot 10^{-4}$	$4.13 \cdot 10^{-6}$	$(8.6 \cdot 10^{-4} - 8.81 \cdot 10^{-4})$
α_1 [s^{-1}]	0.0	100.0	56.59	25.33	$(7 - 100)$
α_1 [s^{-1}]	0.0	100.0	48.12	29.48	$(0 - 100)$
α_1 [s^{-1}]	0.0	100.0	$1.68 \cdot 10^{-4}$	$7.8 \cdot 10^{-6}$	$(1.52 \cdot 10^{-4} - 1.83 \cdot 10^{-4})$
α_L [cm]	0.0	3.0	0.87	0.015	$(0.84 - 0.90)$

The MCMC sampler reaches convergence after approximately 20,000 model runs. **Fig. 5** shows the posterior parameter distributions and the pairwise correlations in the MCMC sample.

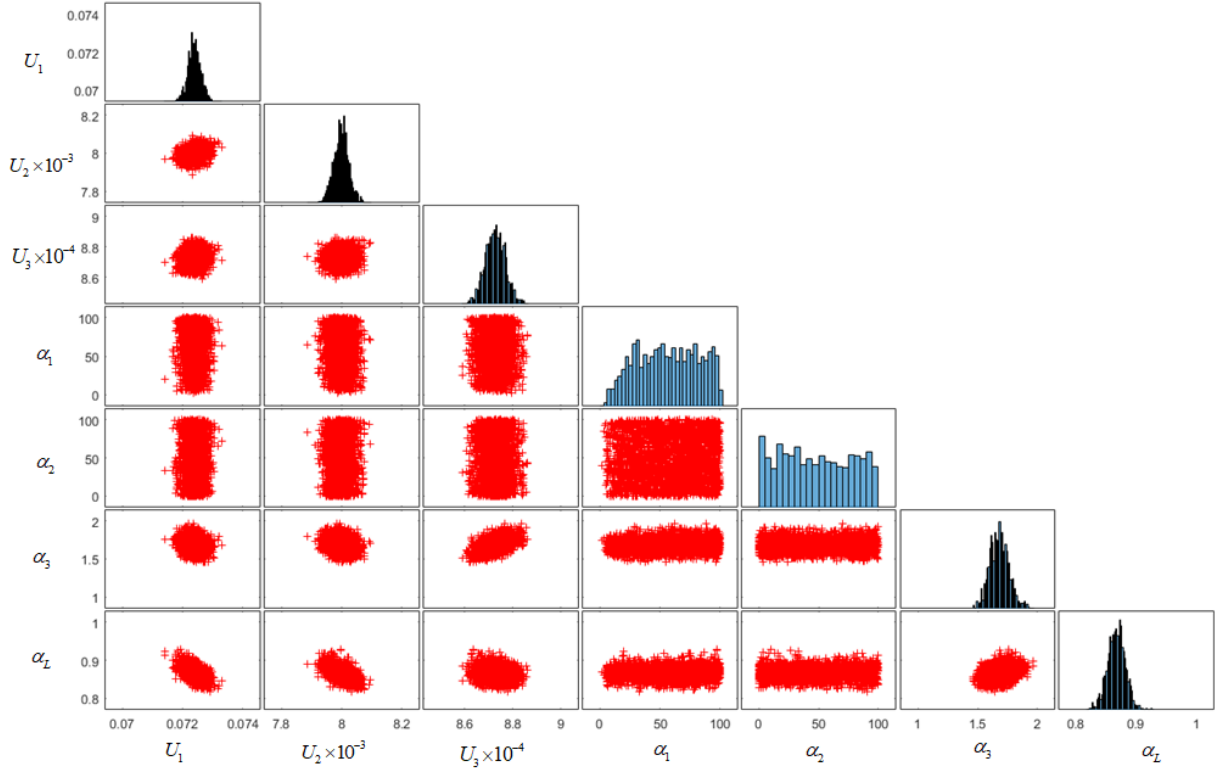


Fig. 5. MCMC solution for the FOMIM model. The diagonal plots represent the posterior distribution of the parameters. The off-diagonal scatterplots represent the correlations in the MCMC draws.

The results of **Fig. 5** show that there is no correlation between the seven parameters. Further, five parameters are well estimated corresponding to the three velocities, the dispersion coefficient and the last transfer coefficient (that of the slow flow rate experiment). All these five parameters have bell-shaped posterior distributions in the diagonal plots of **Fig. 5**. The posterior distributions of the transfer coefficients corresponding to the fast and medium flow rate experiments given in the diagonal plots of **Fig. 5** show almost uniform distributions. The results of the Bayesian calibration given in **Table 3** show that the three velocities are estimated with small confidence intervals, although the mean estimated values are significantly different from the estimated values using the ADE model (**Table 1**). The posterior confidence intervals of the transfer coefficients of the fast and medium flow rate experiments are almost similar to their prior intervals. This shows that these two parameters are insensitive (they have almost no influence on the BTCs). The transfer coefficient of the slow flow rate experiment is very

sensitive since its posterior interval is strongly reduced compared to the prior interval and as a consequence, the parameter is well identified.

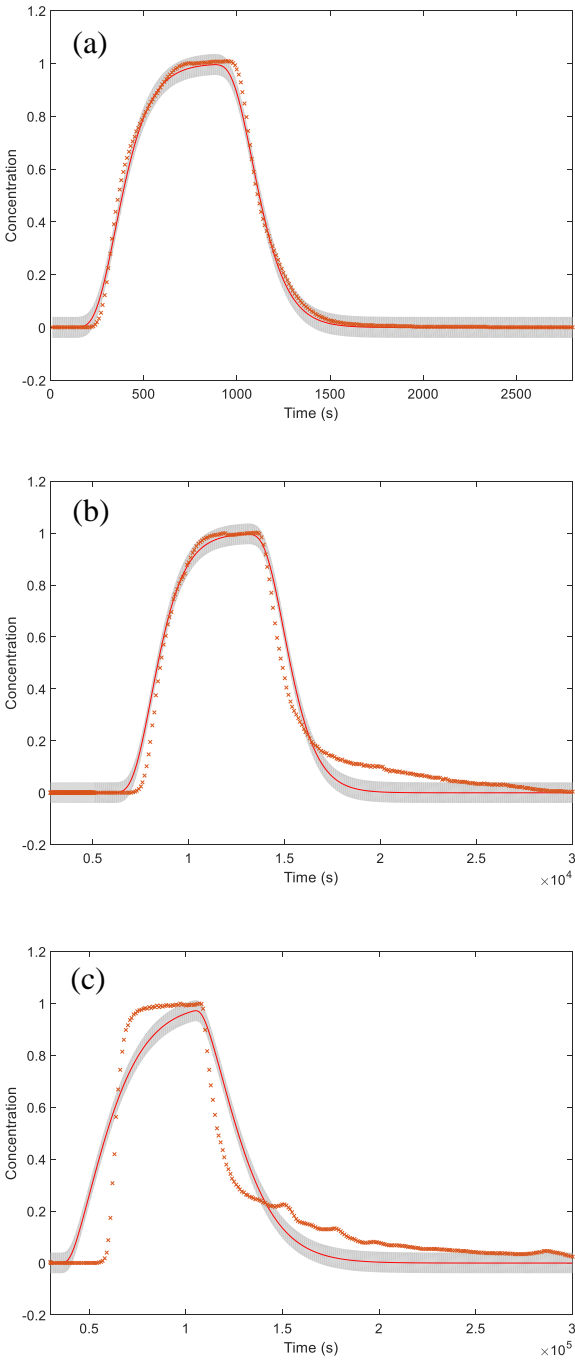


Fig. 6. Observed concentrations (dots), calibrated solution corresponding to the MAP (lines), and predictive uncertainty (grey band) with the FOMIM model for the fast (a), medium (b), and slow (c) flow rate experiments.

1 Compared to the ADE model, the sum of the squares of differences between the observed and
2 predicted concentrations for the three experiments with the FOMIM model reduces by only 8%
3 and the BIC by only 12% (**Table 1**). The measured breakthrough curves as well as the calibrated
4 concentrations and the predictive uncertainty obtained with the FOMIM model are depicted in
5 **Fig. 6**. The results of the fast and slow flow rate experiments are similar to those of the ADE
6 model in **Fig. 4**. A satisfactory fitting is obtained for the fast flow rate experiment (**Fig. 6a**),
7 whereas, the BTC of the medium flow rate experiment (**Fig.6b**) is less well reproduced,
8 especially the tail of the curve. For the slow flow rate experiment, compared to the ADE model,
9 the FOMIM model allows to better reproduce the tail of the measured BTC. However it fails to
10 well reproduce the first sharp front. As a consequence, the overall fitting of this experiment is
11 not satisfactory and **Fig. 6c** shows strong discrepancies between measured and observed BTCs.

27 **3.3 Parameter Estimation for the NLMIM Model**

28 The nonlinear model includes an immobile phase and two associated transfer parameters (λ
29 and μ , see Eq. 3) in addition to the single mobile phase of the linear model. The transfer
30 parameters are a priori assumed uniformly distributed over the large intervals (between 0 and
31 50, see **Table 4**). Two scenarios are investigated. In the first, the transfer coefficient λ is
32 assumed constant for the three flow rate experiments, whereas in the second scenario, λ may
33 depend on the mean flow velocity (as for the parameter α with the FOMIM model).

34 In the case considering that the transfer parameter should be constant, irrespective of the
35 velocity in the mobile phase, the MCMC sampler reaches convergence after approximately
36 25,000 model runs. **Fig. 7** shows the posterior parameter distributions and the pairwise
37 correlations in the MCMC sample. All parameters show almost bell-shaped posterior
38 distributions. Moderate correlations are observed between the three velocities: between U_1 and
39 U_2 ($r=0.93$), between U_1 and U_3 ($r=0.91$) and, between U_2 and U_3 ($r=0.91$). The
40
41
42
43
44
45
46
47
48
49
50
51
52
53
54
55
56
57
58
59
60
61
62
63
64
65

parameter μ has small correlations to U_1 ($r=-0.83$), U_2 ($r=-0.82$), U_3 ($r=-0.82$) and to λ ($r=0.83$).

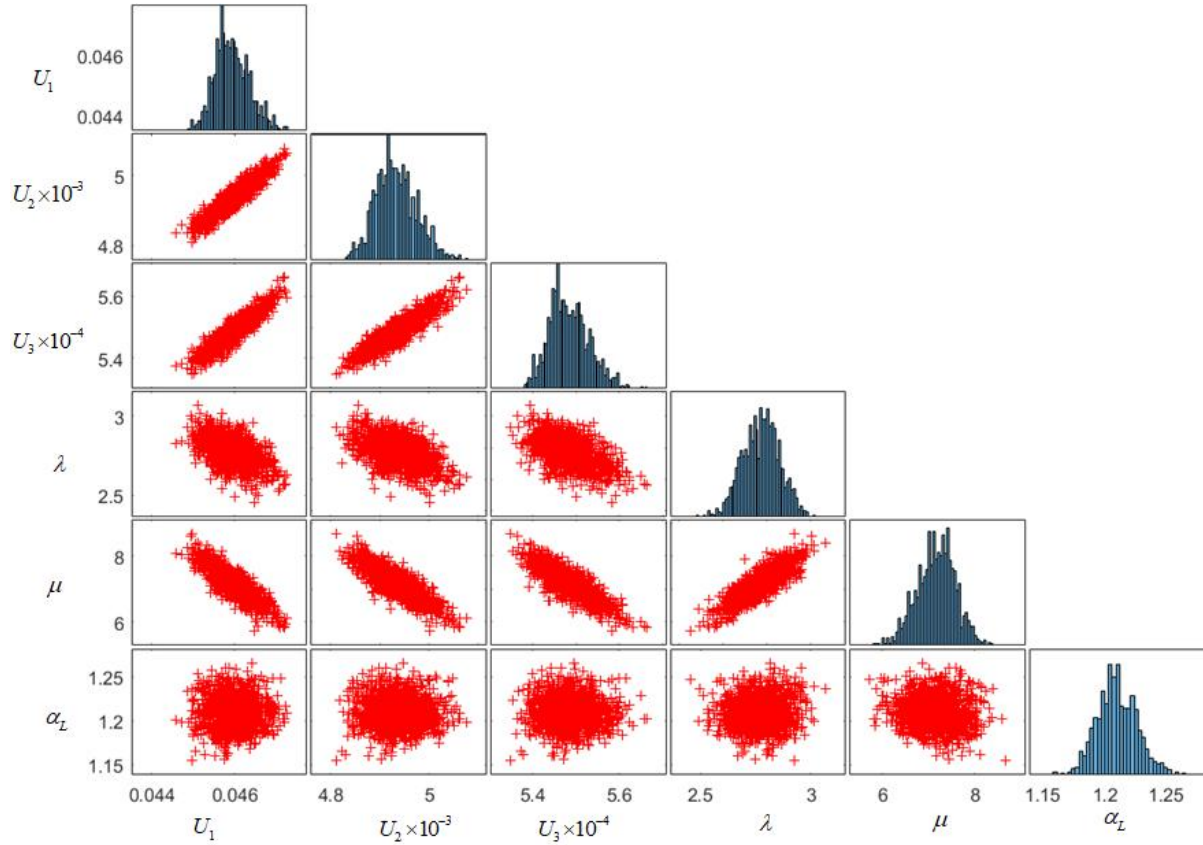


Fig. 7. MCMC solution for the NLMIM model. The diagonal plots represent the posterior distribution of the parameters. The off-diagonal scatterplots represent the correlations in the MCMC draws.

The results of the Bayesian calibration given in **Table 4** show that the six parameters are well estimated with narrow confidence intervals. **Fig. 8** shows measured breakthrough curves compared with calibrated concentrations, and the predictive uncertainty obtained with the NLMIM model.

Table 4. Prior intervals and estimated mean values and confidence intervals (CIs) for the parameters of the NLMIM model.

Parameters	Prior intervals		Estimations		
	Lower bound	Upper bound	Mean	Standard deviation	95% Confidence Interval
U_1 [cm/s]	0.03	0.1	$4.59 \cdot 10^{-2}$	$4.08 \cdot 10^{-4}$	$(4.51 \cdot 10^{-2} - 4.67 \cdot 10^{-2})$
U_2 [cm/s]	0.003	0.01	$4.93 \cdot 10^{-3}$	$4.17 \cdot 10^{-5}$	$(4.85 \cdot 10^{-3} - 5.02 \cdot 10^{-3})$
U_3 [cm/s]	0.0003	0.001	$5.48 \cdot 10^{-4}$	$4.59 \cdot 10^{-6}$	$(5.39 \cdot 10^{-4} - 5.57 \cdot 10^{-4})$
λ [s ⁻¹]	0.0	50.0	2.77	$8.4 \cdot 10^{-2}$	(2.61 – 2.94)
μ [-]	0.0	50.0	7.17	$4.15 \cdot 10^{-1}$	(6.36 – 7.99)
α [cm]	0.0	3.0	1.21	$1.62 \cdot 10^{-2}$	(1.18 – 1.24)

In **Fig. 8b**, the second experiment with the medium flow rate is very well reproduced by the numerical model, with a tail of the breakthrough curve well reproduced by the NLMIM model compared with rough results from the ADE and FOMIM models (see **Fig. 4b** and **Fig. 6b**). However, the first experiment, with the fast flow rate (**Fig. 8a**), is not as well reproduced as by the ADE model (**Fig. 4a**) because the NLMIM model generates a short concentration tail not observed on the measured concentrations. In opposition, the third experiment with the slow flow rate (**Fig. 8c**) is better reproduced by the NLMIM model than the ADE and FOMIM models (**Fig. 4c** and **Fig. 6c**). Nevertheless, the tail of the simulated breakthrough in **Fig. 8c** is spread enough over time, but there is not enough mass to mimic the high concentration values observed in the experimental breakthrough curve. With a NLMIM model correctly simulating medium velocity breakthroughs, overestimating late concentration values at high fluid velocity, and underestimating late concentrations at small velocity, the model is still performing better than the ADE and FOMIM models. The feature is exemplified by the squared differences between the observed and predicted concentrations at the MAP; compared to the ADE model, it is reduced by 40%, and the BIC is significantly decreased from 9173 to 2862 (**Table 2**).

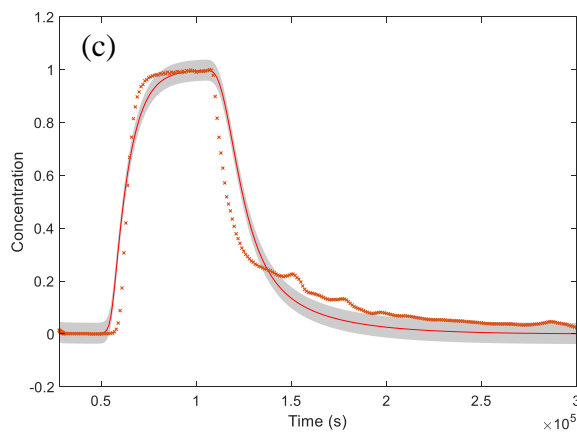
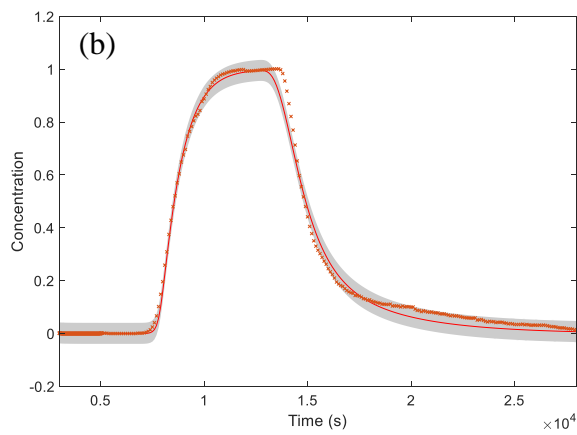
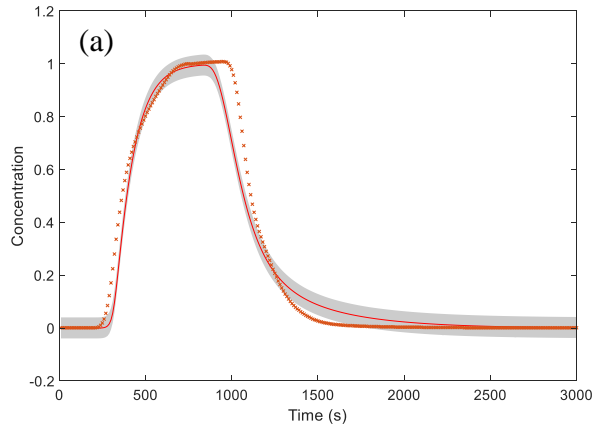


Fig. 8. Observed concentrations (dots), calibrated solution corresponding to the MAP (lines), and predictive uncertainty (grey band) with the NLMIM model for the fast (a), medium (b), and slow (c) flow rate experiments.

3.4. Parameter Estimation for the NLMIM Model with Variable Coefficient

In this case, the coefficient λ is assumed to vary according to the fluid velocity in the column.

The nonlinear model is therefore calibrated using three transfer coefficients λ_1 , λ_2 and λ_3 respectively attributed to the fast, medium, and slow flow rate experiments. The three coefficients have prior uniform distributions over the same large interval [0-50].

With additional parameters, the MCMC sampler requires more model runs to reach the convergence, here approximately 40,000 runs. **Fig. 9** shows the posterior parameter distributions and the pairwise correlations obtained with the converged MCMC samples. All parameters show almost bell-shaped posterior distributions (**Fig. 9**). Moderate correlations are observed between U_1 and λ_1 ($r=0.75$), U_3 and μ ($r=-0.81$), and λ_2 , and μ ($r=0.76$).

The results of the Bayesian calibration given in **Table 5** show that the eight parameters are well estimated with narrow confidence intervals. **Fig. 10** shows that the calibrated model correctly fits data from the measured breakthrough curves for the three velocities investigated by the experiments, with uncertainties on simulations (gray areas in **Fig. 10**) tightly bounding the observed concentration breakthroughs. The overall quality of the estimation has been significantly improved, with a squared difference between the observed and predicted concentrations at the MAP 6 times smaller than that of the previous nonlinear model with fixed λ . The BIC is also significantly reduced from 2862 to -4557 (**Table 2**).

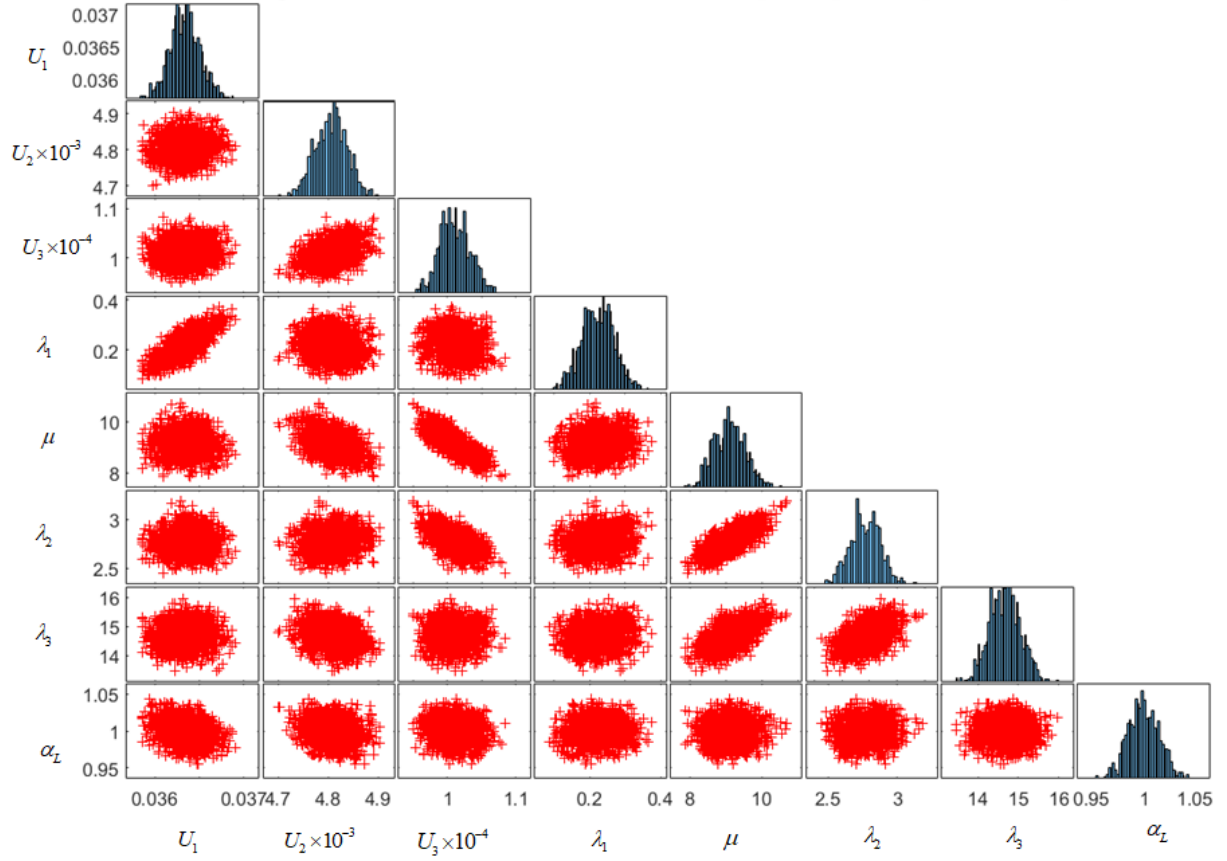


Fig. 9. Observed concentrations (symbols), calibrated solution corresponding to the MAP (lines), and predictive uncertainty (grey band) with the NLMIM model and variable coefficients λ for the three experiments.

Table 5. Prior intervals and estimated mean values and confidence intervals (CIs) for the parameters of the NLMIM model with variable coefficients λ .

Parameters	Prior intervals		Estimations		
	Lower bound	Upper bound	Mean	Standard deviation	95% Confidence Interval
U_1 [cm/s]	0.03	0.1	$3.63 \cdot 10^{-2}$	$1.69 \cdot 10^{-4}$	$(3.6 \cdot 10^{-2} - 3.67 \cdot 10^{-2})$
U_2 [cm/s]	0.003	0.01	$4.81 \cdot 10^{-3}$	$3.19 \cdot 10^{-5}$	$(4.74 \cdot 10^{-3} - 4.87 \cdot 10^{-3})$
U_3 [cm/s]	0.0003	0.001	$1.01 \cdot 10^{-5}$	$2.2 \cdot 10^{-5}$	$(9.68 \cdot 10^{-4} - 1.05 \cdot 10^{-3})$
λ_1 [s $^{-1}$]	0.0	50.0	$2.23 \cdot 10^{-1}$	$4.64 \cdot 10^{-2}$	$(1.32 \cdot 10^{-1} - 3.14 \cdot 10^{-1})$
λ_2 [s $^{-1}$]	0.0	50.0	2.77	$1.08 \cdot 10^{-1}$	$(2.56 - 2.98)$
λ_3 [s $^{-1}$]	0.0	50.0	14.7	$3.81 \cdot 10^{-1}$	$(13.9 - 15.4)$
μ [-]	9.11	$4.39 \cdot 10^{-1}$	9.11	$4.39 \cdot 10^{-1}$	$(8.25 - 9.97)$
α [cm]	0.0	3.0	1.0	$1.49 \cdot 10^{-2}$	$(0.97 - 1.03)$

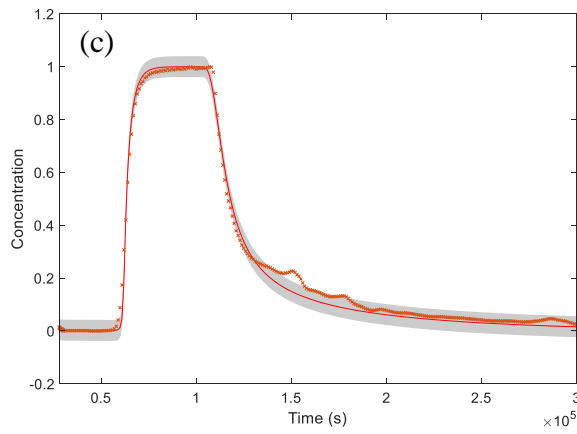
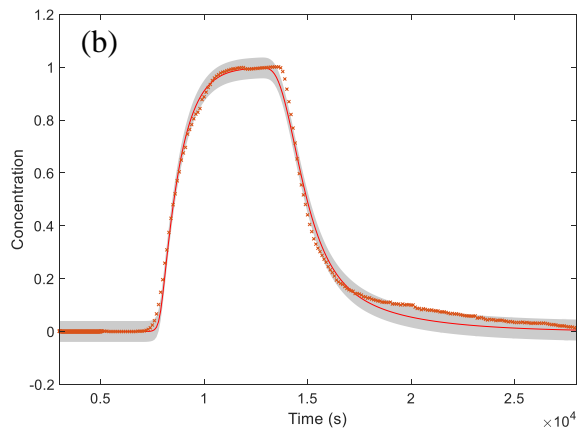
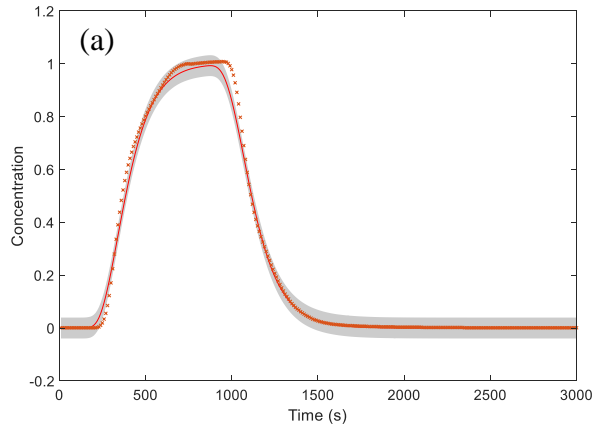


Fig. 10. Observed concentrations (dots), calibrated solution corresponding to the MAP (lines), and predictive uncertainty (grey band) with the NLMIM model and variable coefficients λ for the fast (a), medium (b), and slow (c) flow rate experiments.

4. Summary and Conclusions

Simulation of transport through fractured porous media is challenging since most of water and contaminant travel through the fractures whose properties (such as location, shape, orientation, size and aperture) are generally unknown. In this work, we conducted laboratory experiments with a novel setup in which a column filled with glass beads and parallelepiped-shaped limestone beams was used to reconstruct a medium with multiple small fractures (at the scale of a hand-size rock sample). Three lab-scale experiments were conducted to investigate saline tracer BTCs in the case of fast, medium, and slow flow rates through the fractured medium. Three transport models have been investigated for the inversion of the measured BTCs. The first transport model (ADE) corresponds to the linear advection dispersion equation. The second model (FOMIM), is based on the mobile/immobile approach and uses a linear first-order transfer function between mobile and immobile zones, whereas the third model (NLMIM), uses a nonlinear transfer function between the fractures and the matrix. Inversion of the three transport models is performed using Bayesian MCMC inference. Key findings of the current study can be summarized as follows:

1. The proposed multi-fracture experimental setup can produce asymmetric BTCs that are consistent with past field- and lab-scale studies.
2. All the unknown parameters of the ADE model can be well-estimated with narrow confidence intervals. With respect to state estimation, the ADE model can reproduce with fair precision the BTC obtained under fast flow conditions but fails to reproduce the tails of the BTCs observed with the medium and slow flow rate experiments.
3. The FOMIN model improves the tailing of the BTCs but significant discrepancies remain between simulated and measured concentrations. The first-order transfer coefficients of the fast and medium flow rate experiment are insensitive and cannot be

1
2
3
4
5
6
7
8
9
10
11
12
13
14
15
16
17
18
19
20
21
22
23
24
25
26
27
28
29
30
31
32
33
34
35
36
37
38
39
40
41
42
43
44
45
46
47
48
49
50
51
52
53
54
55
56
57
58
59
60
61
62
63
64
65

estimated from the BTCs contrarily to the transfer coefficient of the slow flow rate experiment which is well identified.

4. The NLMIM model with a constant (kinetic) coefficient λ has better performance in simulating the medium flow BTC, but performs worse for the fast flow conditions as it overestimates the concentration values characterizing the tail of the BTC.
5. The nonlinear model with a velocity-dependent λ coefficient is the only model correctly capturing the experimental BTCs under all three conditions of fast, medium, and slow flow rates. All its parameters are well estimated with narrow confidence intervals.

The experimental results presented in this paper could be used to validate and analyze other inversion and data assimilation methods applicable to fracture parameter estimation. Future studies may consider sequential Bayesian filtering and smoothing methods, which have been less considered in this context. The proposed experimental setup can serve as a basic platform to investigate less-explored phenomena related to transport in limestone fractures, such as non-aqueous phase and colloid transport.

References

Abdelaziz, R., & Merkel, B. J. (2015). Sensitivity analysis of transport modeling in a fractured gneiss aquifer. *Journal of African Earth Sciences*, *103*, 121-127.

Arnold, D. N., Brezzi, F., Cockburn, B., & Marini, L. D. (2002). Unified analysis of discontinuous Galerkin methods for elliptic problems. *SIAM journal on numerical analysis*, *39*(5), 1749-1779.

Brissaud, F., Pappalardo, A., & Peaudecerf, P. (1978). Transferts dispersifs dans une tranche verticale de milieu aquifere. In *Symposium" les effets d'echelle en milieu poreux"*, Thessaloniki, September (pp. 2-23).

Coats, K. H., & Smith, B. D. (1964). Dead-end pore volume and dispersion in porous media. *Society of petroleum engineers journal*, *4*(01), 73-84.

1
2
3
4
5
6
7
8
9
10
11
12
13
14
15
16
17
18
19
20
21
22
23
24
25
26
27
28
29
30
31
32
33
34
35
36
37
38
39
40
41
42
43
44
45
46
47
48
49
50
51
52
53
54
55
56
57
58
59
60
61
62
63
64
65

Fahs, M., Carrayrou, J., Younes, A., & Ackerer, P. (2008). On the efficiency of the direct substitution approach for reactive transport problems in porous media. *Water, air, and soil pollution*, 193(1), 299-308.

Field, M. S., & Leij, F. J. (2012). Solute transport in solution conduits exhibiting multi-peaked breakthrough curves. *Journal of hydrology*, 440, 26-35.

Fiori, A., & Becker, M. W. (2015). Power law breakthrough curve tailing in a fracture: The role of advection. *Journal of Hydrology*, 525, 706-710.

Ford, D., & Williams, P. D. (2013). *Karst hydrogeology and geomorphology*. John Wiley & Sons.

Florea, L. J., & Wicks, C. M. (2001). Solute transport through laboratory-scale karstic aquifers. *Geography/Geology Faculty Publications*, 11.

Gelman, A., & Rubin, D. B. (1992). Inference from iterative simulation using multiple sequences. *Statistical science*, 7(4), 457-472.

Gelman, A., Carlin, J. B., Stern, H. S., & Rubin, D. B. (1995). *Bayesian data analysis*. Chapman and Hall/CRC.

Godlewski, E., & Raviart, P. A. (1996). *Numerical approximation of hyperbolic systems of conservation laws* (Vol. 118, pp. viii+-509). New York: Springer.

Goldscheider, N., Meiman, J., Pronk, M., & Smart, C. (2008). Tracer tests in karst hydrogeology and speleology. *International Journal of speleology*, 37(1), 27-40.

Goldscheider, N., & Drew, D. (Eds.). (2014). *Methods in Karst Hydrogeology: IAH: International Contributions to Hydrogeology*, 26. Crc Press.

Guo, Z., Henri, C. V., Fogg, G. E., Zhang, Y., & Zheng, C. (2020). Adaptive Multirate Mass Transfer (aMMT) model: A new approach to upscale regional- scale transport under transient flow conditions. *Water Resources Research*, 56(2), e2019WR026000.

Hartmann, A., Goldscheider, N., Wagener, T., Lange, J., & Weiler, M. (2014). Karst water resources in a changing world: Review of hydrological modeling approaches. *Reviews of Geophysics*, 52(3), 218-242.

Hauns, M., Jeannin, P. Y., & Atteia, O. (2001). Dispersion, retardation and scale effect in tracer breakthrough curves in karst conduits. *Journal of hydrology*, 241(3-4), 177-193.

1 Hawkins, A. J., Fox, D. B., Koch, D. L., Becker, M. W., & Tester, J. W. (2020). Predictive
2 Inverse Model for Advective Heat Transfer in a Short- Circuited Fracture: Dimensional
3 Analysis, Machine Learning, and Field Demonstration. *Water Resources Research*, 56(11),
4 e2020WR027065.
5

6
7 Helmke, M. F., Simpkins, W. W., & Horton, R. (2005). Simulating conservative tracers in
8 fractured till under realistic timescales. *Groundwater*, 43(6), 877-889.
9

10
11 Herr, M., Schäfer, G., & Spitz, K. (1989). Experimental studies of mass transport in porous
12 media with local heterogeneities. *Journal of contaminant hydrology*, 4(2), 127-137.
13

14
15 Huyakorn, P. S., & Pinder, G. F. (1983). *Computational Methods in Subsurface Flow*.
16 Academic Press.
17

18
19 Kirby, R. C. (2000). Local time stepping and a posteriori error estimates for flow and
20 transport in porous media. The University of Texas at Austin.
21

22
23 Jørgensen, P. R., Helstrup, T., Urup, J., & Seifert, D. (2004). Modeling of non-reactive solute
24 transport in fractured clayey till during variable flow rate and time. *Journal of Contaminant*
25 *Hydrology*, 68(3-4), 193-216.
26

27
28 Labat, D., & Mangin, A. (2015). Transfer function approach for artificial tracer test
29 interpretation in karstic systems. *Journal of Hydrology*, 529, 866-871.
30

31
32 Li, G. (2004). Laboratory simulation of solute transport and retention in a karst aquifer.
33 Doctoral dissertation, The Florida State University.
34

35
36 Li, G., Loper, D. E., & Kung, R. (2008). Contaminant sequestration in karstic aquifers:
37 Experiments and quantification. *Water Resources Research*, 44(2).
38

39
40 Li, L., Jiang, H., Wu, K., Li, J., & Chen, Z. (2019). An analysis of tracer flowback profiles
41 to reduce uncertainty in fracture-network geometries. *Journal of Petroleum Science and*
42 *Engineering*, 173, 246-257.
43

44
45 Linde, N., Ginsbourger, D., Irving, J., Nobile, F., & Doucet, A. (2017). On uncertainty
46 quantification in hydrogeology and hydrogeophysics. *Advances in Water Resources*, 110, 166-
47 181.
48

49
50 Liu, Y., Liu, Y., Luo, Q., Li, H., & Qian, J. (2021). Experimental and numerical study of
51 bimolecular reactive transport in a single rough-wall fracture. *Journal of Hydrology*, 594,
52 125944.
53

1
2
3
4
5
6
7
8
9
10
11
12
13
14
15
16
17
18
19
20
21
22
23
24
25
26
27
28
29
30
31
32
33
34
35
36
37
38
39
40
41
42
43
44
45
46
47
48
49
50
51
52
53
54
55
56
57
58
59
60
61
62
63
64
65

Massei, N., Wang, H. Q., Field, M. S., Dupont, J. P., Bakalowicz, M., & Rodet, J. (2006). Interpreting tracer breakthrough tailing in a conduit-dominated karstic aquifer. *Hydrogeology Journal*, 14(6), 849-858.

Mohammadi, Z., Gharaat, M. J., & Field, M. (2019). The Effect of Hydraulic Gradient and Pattern of Conduit Systems on Tracing Tests: Bench- Scale Modeling. *Groundwater*, 57(1), 110-125.

Morales, T., de Valderrama, I. F., Uriarte, J. A., Antigüedad, I., & Olazar, M. (2007). Predicting travel times and transport characterization in karst conduits by analyzing tracer-breakthrough curves. *Journal of hydrology*, 334(1-2), 183-198.

Moreira, P. H., Van Genuchten, M. T., Orlande, H. R., & Cotta, R. M. (2016). Bayesian estimation of the hydraulic and solute transport properties of a small-scale unsaturated soil column. *Journal of Hydrology and Hydromechanics*, 64(1), 30-44.

Nikan, O., Machado, J. T., Golbabai, A., & Nikazad, T. (2020). Numerical approach for modeling fractal mobile/immobile transport model in porous and fractured media. *International Communications in Heat and Mass Transfer*, 111, 104443.

Palmer, A., Palmer, M., & Sasowsky, I. (Eds.). (1999). *Karst modeling* (Vol. 5). Karst Waters Institute. p. 176.

Pastore, N. (2018). Fluid Flow, Mass, and Heat Transport Laboratory Experiments in Artificially Fractured Rock. *Hydrology of Artificial and Controlled Experiments*. In: Liu, J., Gu, W. editors. London: IntechOpen.

Qian, J., Zhan, H., Zhao, W., & Sun, F. (2005). Experimental study of turbulent unconfined groundwater flow in a single fracture. *Journal of Hydrology*, 311(1-4), 134-142.

Rajabi, M. M., & Ataie-Ashtiani, B. (2016). Efficient fuzzy Bayesian inference algorithms for incorporating expert knowledge in parameter estimation. *Journal of Hydrology*, 536, 255-272.

Rajabi, M. M., Ataie-Ashtiani, B., & Simmons, C. T. (2018). Model-data interaction in groundwater studies: Review of methods, applications and future directions. *Journal of hydrology*, 567, 457-477.

1 Schöniger, A., Wöhling, T., Samaniego, L., & Nowak, W. (2014). Model selection on solid
2 ground: Rigorous comparison of nine ways to evaluate Bayesian model evidence. *Water*
3 *Resources Research*, 50(12), 9484-9513.
4

5 Schwarz, G. (1978). Estimating the dimension of a model. *The annals of statistics*, 461-464.
6

7 Siegel, P., Mosé, R., Ackerer, P., & Jaffré, J. (1997). Solution of the advection–diffusion
8 equation using a combination of discontinuous and mixed finite elements. *International journal*
9 *for numerical methods in fluids*, 24(6), 595-613.
10

11 Somogyvári, M., Jalali, M., Jimenez Parras, S., & Bayer, P. (2017). Synthetic fracture
12 network characterization with transdimensional inversion. *Water Resources Research*, 53(6),
13 5104-5123.
14

15 Tu, S., & Aliabadi, S. (2005). A slope limiting procedure in discontinuous Galerkin finite
16 element method for gasdynamics applications. *International Journal of Numerical Analysis and*
17 *Modeling*, 2(2), 163-178.
18

19 Vrugt, J. A., Gupta, H. V., Bouten, W., & Sorooshian, S. (2003). A Shuffled Complex
20 Evolution Metropolis algorithm for optimization and uncertainty assessment of hydrologic
21 model parameters. *Water Resources Research*, 39(8).
22

23 Wang, X., Jardani, A., & Jourde, H. (2017). A hybrid inverse method for hydraulic
24 tomography in fractured and karstic media. *Journal of Hydrology*, 551, 29-46.
25

26 Wang, C., Wang, X., Majdalani, S., Guinot, V., & Jourde, H. (2020). Influence of dual
27 conduit structure on solute transport in karst tracer tests: An experimental laboratory study.
28 *Journal of Hydrology*, 590, 125255.
29

30 Wu, Y. S., Liu, H. H., & Bodvarsson, G. S. (2004). A triple-continuum approach for
31 modeling flow and transport processes in fractured rock. *Journal of Contaminant Hydrology*,
32 73(1-4), 145-179.
33

34 Younes, A., & Ackerer, P. (2008). Solving the advection–dispersion equation with
35 discontinuous Galerkin and multipoint flux approximation methods on unstructured meshes.
36 *International Journal for Numerical Methods in Fluids*, 58(6), 687-708.
37

38 Younes, A., Fahs, M., & Ackerer, P. (2010). An efficient geometric approach to solve the
39 slope limiting problem with the discontinuous Galerkin method on unstructured triangles.
40 *International Journal for Numerical Methods in Biomedical Engineering*, 26(12), 1824-1835.
41

1
2
3
4
5
6
7
8
9
10
11
12
13
14
15
16
17
18
19
20
21
22
23
24
25
26
27
28
29
30
31
32
33
34
35
36
37
38
39
40
41
42
43
44
45
46
47
48
49
50
51
52
53
54
55
56
57
58
59
60
61
62
63
64
65

Younes, A., Delay, F., Fajraoui, N., Fahs, M., & Mara, T. A. (2016). Global sensitivity analysis and Bayesian parameter inference for solute transport in porous media colonized by biofilms. *Journal of contaminant hydrology*, 191, 1-18.

Zhang, C., Shu, L., Appiah-Adjei, E. K., Lobeyo, A. G., Tang, R., & Fan, J. (2016). Laboratory simulation of groundwater hydraulic head in a karst aquifer system with conduit and fracture domains. *Carbonates and Evaporites*, 31(3), 329-337.

Zhao, X., Chang, Y., Wu, J., & Peng, F. (2017). Laboratory investigation and simulation of breakthrough curves in karst conduits with pools. *Hydrogeology Journal*, 25(8), 2235-2250.

Zhao, X., Chang, Y., Wu, J., & Xue, X. (2019). Effects of flow rate variation on solute transport in a karst conduit with a pool. *Environmental Earth Sciences*, 78(7), 1-18.

Zhou, Z., Roubinet, D., & Tartakovsky, D. M. (2021). Thermal experiments for fractured rock characterization: theoretical analysis and inverse modeling. *Water Resources Research*, 57(12), e2021WR030608.

Zhu, L., Li, L., & Liang, Z. (2009). Comparison of six statistical approaches in the selection of appropriate fish growth models. *Chinese Journal of Oceanology and Limnology*, 27(3), 457.

Zoghbi, C., & Basha, H. (2020). Simple transport models for karst systems. *Journal of Hydrology*, 588, 125046.